Tachyon optics: Kirchhoff identities and superluminal Bragg diffraction

Roman Tomaschitz *

Department of Physics, Hiroshima University, 1-3-1 Kagami-yama, Higashi-Hiroshima 739-8526, Japan

ARTICLE INFO

ABSTRACT

The diffraction of superluminal radiation fields in crystal lattices is studied. The negative mass-square of the tachyonic wave modes affects the modulation function of diffraction gratings and the scattering amplitude. The Bragg condition for tachyon diffraction as well as the longitudinal and transversal cross sections are derived. Scalar and vectorial Kirchhoff identities for superluminal Proca fields are obtained from Sommerfeld's dipole functionals, in analogy to electromagnetic theory. These surface-integral representations of the tachyon potential and the tachyonic field strengths are used to calculate the asymptotic diffracted modes and the intensity ratios. The dependence of the primary and secondary intensity peaks on the tachyon mass is analyzed in the reciprocal lattice, and the conversion of transversal into longitudinal radiation by way of Bragg scattering is explained. Specifically, tachyonic spectral fits are performed to the TeV spectra of three active galactic nuclei, H2356 − 309, 1ES 1218 + 304, and 1ES 1101 − 232, obtained with the imaging atmospheric Cherenkov detectors HESS, MAGIC, and VERITAS. The curvature in the spectral maps of these blazars is shown to be intrinsic, generated by ultra-relativistic electron populations in the galactic nuclei rather than by intergalactic absorption, and is reproduced by a tachyonic cascade fit.

1. Introduction

We investigate the diffraction of superluminal wave modes, outlining a theory of tachyon diffraction based on Kirchhoff's surface-integral representation of Proca fields. We work out two specific examples, diffraction at plane apertures such as diffraction gratings, and tachyonic Bragg scattering in crystal lattices. The formalism is developed in close analogy to electromagnetic diffraction theory, even though there are substantial differences owing to the negative mass-square of tachyons [1–5] and the occurrence of longitudinally polarized modes [6–8].

The negative mass-square refers to the radiation rather than the source. This in strong contrast to the traditional approach based on superluminal source particles emitting electromagnetic radiation [9]. The tachyonic radiation discussed here implies superluminal energy transfer, the radiation quanta moving faster than light, in contrast to the rotating superluminal light sources studied in Refs. [10–12] and the vacuum Cherenkov radiation suggested in [13–16]. Tachyons are radiation modes, a kind of photons with negative mass-square, coupled by minimal substitution to the electron

current, cf. Section 2. The tachyonic Maxwell equations admit a static potential analogous to the Coulomb potential, but oscillating because of the negative mass-square, and much weaker due to the small tachyonic fine structure constant [17]. Photons can only be radiated by accelerated charges, in contrast to tachyonic quanta, where the emission rate primarily depends on the electronic Lorentz factor rather than on acceleration [18]. Here, we investigate how the intensity peaks and scattering cross sections are affected by the tachyon mass, and study the effect of diffraction on the polarization of superluminal modes. We disentangle the transversal and longitudinal polarization components in the spectral maps of the BL Lacertae objects H2356 − 309, 1ES 1218 + 304, and 1ES 1101 − 232, and show that the TeV spectra of these blazars can be fitted with tachyonic cascades radiated by the thermal electron plasma in the active galactic nuclei. In the spectral maps, the tachyon–electron mass ratio enters in the cutoff energy of the cascades.

In Section 2, we discuss the tachyonic Maxwell equations in Fourier space, including the material equations relating tachyonic inductions and field strengths. We calculate the superluminal radiation fields generated by dipole currents, and introduce dipole functionals to derive the Kirchhoff identities for the scalar and vector potentials as well as the tachyonic field strengths. In Section 3, we study tachyon diffraction at a plane aperture, calculate the

* Tel.: +81 824 247361; fax: +81 824 240717.
  E-mail address: tom@geminga.org

asymptotic diffracted wave modes in the far-field regime, and assemble the intensity ratios determining the conversion efficiency from transversal to longitudinal radiation and vice versa. In Section 4, we consider the specific case of a grating aperture, and calculate the modulation function, from which the intensity peaks of the diffracted superluminal wave fields can be read off. We discuss Bragg diffraction of tachyons in crystal lattices, in particular the effect of the negative mass-square on the transversal and longitudinal scattering cross sections. In Section 5, we perform tachyonic cascade fits to blazar spectra, separate the transversal and longitudinal flux components, and derive estimates of the electronic source populations in the active galactic nuclei. In Section 6, we present our conclusions with regard to tachyonic X-ray spectra obtained with Bragg gratings.

2. Superluminal radiation fields

2.1. Proca equation with negative mass-square

The tachyonic radiation field in vacuum is a real vector field with negative mass-square, satisfying the Proca equation $(\partial^\nu\partial_\nu + m_t^2)A_\mu = -j_\mu$, subject to the Lorentz condition $A^\mu{}_{,\mu} = 0$ [6]. m_t is the mass of the superluminal Proca field A_μ, and q the tachyonic charge carried by the subluminal electron current $j^\mu = (\rho, \mathbf{j})$. In the Proca equation, the mass term is added with a positive sign, and the sign convention for the metric defining the d'Alembertian $\partial^\nu\partial_\nu$ is diag$(-1, 1, 1, 1)$, so that $m_t^2 > 0$ is the negative mass-square of the radiation field. The 3D version of Proca's equation is a set of Maxwell equations,

$$\operatorname{div}\mathbf{B}(\mathbf{x}, t) = 0, \quad \operatorname{rot}\mathbf{E} + \partial\mathbf{B}/\partial t = 0,$$
$$\operatorname{div}\mathbf{E} = \rho - m_t^2 A_0, \quad \operatorname{rot}\mathbf{B} - \partial\mathbf{E}/\partial t = \mathbf{j} + m_t^2\mathbf{A},$$
(2.1)

where the field strengths are related to the potential by $\mathbf{E} = \nabla A_0 - \partial\mathbf{A}/\partial t$ and $\mathbf{B} = \operatorname{rot}\mathbf{A}$. The Lorentz condition, $\operatorname{div}\mathbf{A} - \partial A_0/\partial t = 0$, follows from the field equations and current conservation, $\operatorname{div}\mathbf{j} + \partial\rho/\partial t = 0$.

In a permeable medium, the potential and field strengths in the inhomogeneous vacuum equations are replaced by inductions, $(A_0, \mathbf{A}) \to (C_0, \mathbf{C})$, $(\mathbf{E}, \mathbf{B}) \to (\mathbf{D}, \mathbf{H})$, defined by material equations [19–21]. We will mostly consider monochromatic waves, $\mathbf{A}(\mathbf{x}, t) = \hat{\mathbf{A}}(\mathbf{x}, \omega)e^{-i\omega t} + \text{c.c.}$, and analogously for the scalar potential A_0, the current, charge density, field strengths, and inductions. Fourier amplitudes are denoted by a hat. The tachyonic Maxwell equations (2.1) read in Fourier space as

$$\operatorname{rot}\hat{\mathbf{E}} - i\omega\hat{\mathbf{B}} = 0, \quad \operatorname{div}\hat{\mathbf{B}} = 0,$$
$$\operatorname{rot}\hat{\mathbf{H}} + i\omega\hat{\mathbf{D}} = \hat{\mathbf{j}} + m_t^2\hat{\mathbf{C}}, \quad \operatorname{div}\hat{\mathbf{D}} = \hat\rho - m_t^2\hat{C}_0,$$
(2.2)

supplemented by material equations,

$$\hat{\mathbf{A}}(\omega) = \mu_0(\omega)\hat{\mathbf{C}}(\omega), \quad \hat{C}_0(\omega) = \varepsilon_0(\omega)\hat{A}_0(\omega),$$
$$\hat{\mathbf{D}}(\mathbf{x}, \omega) = \varepsilon(\omega)\hat{\mathbf{E}}(\mathbf{x}, \omega), \quad \hat{\mathbf{B}}(\mathbf{x}, \omega) = \mu(\omega)\hat{\mathbf{H}}(\mathbf{x}, \omega).$$
(2.3)

The inductive potentials $(\hat{C}_0, \hat{\mathbf{C}})$ as well as $\hat{\mathbf{D}}$ and $\hat{\mathbf{H}}$ are related to the primary fields by frequency-dependent dielectric and magnetic permeabilities. In an anisotropic medium, we have to use tensorial permeabilities, e.g. $\hat{A}_i = \mu_{0,ik}\hat{C}_k$. The Fourier amplitudes of the field strengths and potentials are connected by $\hat{\mathbf{E}} = i\omega\hat{\mathbf{A}} + \nabla\hat{A}_0$ and $\hat{\mathbf{B}} = \operatorname{rot}\hat{\mathbf{A}}$. Current conservation, $\operatorname{div}\hat{\mathbf{j}} = i\omega\hat\rho$, implies the Lorentz condition $\operatorname{div}\hat{\mathbf{A}} + i\varepsilon_0\mu_0\omega\hat{A}_0 = 0$. In a dissipative medium, the permittivities $(\varepsilon_0, \varepsilon)$ and permeabilities (μ_0, μ) are complex, resulting in exponential attenuation of the wave fields [22].

2.2. Tachyonic dipole fields

We substitute the potential representation of the field strengths into the inhomogeneous field equations in (2.2), and make use of the Lorentz condition to find

$$\left(\Delta + \varepsilon_0\mu_0\omega^2 + \frac{\varepsilon_0}{\varepsilon}m_t^2\right)\hat{A}_0 = \frac{1}{\varepsilon}\hat\rho,$$
$$\left(\Delta + \varepsilon\mu\omega^2 + \frac{\mu}{\mu_0}m_t^2\right)\hat{\mathbf{A}} + \left(\frac{\varepsilon}{\varepsilon_0}\frac{\mu}{\mu_0} - 1\right)\nabla\operatorname{div}\hat{\mathbf{A}} = -\mu\hat{\mathbf{j}}.$$
(2.4)

We identify $\varepsilon_0 = \varepsilon$ and $\mu_0 = \mu$, otherwise different dispersion relations are obtained for the scalar and vector potentials, implying different group velocities of the transversal and longitudinal modes. On the left-hand side of (2.4), we can thus identify the squared wave number as

$$k^2 = \varepsilon(\omega)\mu(\omega)\omega^2 + m_t^2.$$
(2.5)

We consider real ε, μ, and a positive k^2; the permeabilities may even be negative [23], but then we restrict to a frequency range with positive squared wave numbers. The Green function inverting the wave equations (2.4) is

$$(\Delta + k^2)G(x, x_0; \omega) = -\delta(x - x_0),$$
(2.6)

$$G(x, x_0; \omega) = \frac{\exp(ik|x - x_0|)}{4\pi|x - x_0|}, \quad k = \sqrt{\varepsilon(\omega)\mu(\omega)\omega^2 + m_t^2}.$$
(2.7)

Here, Re $k > 0$, so that $G(x, x_0; \omega)$ gives retarded solutions,

$$(\hat{A}_0(x, \omega), \hat{\mathbf{A}}(x, \omega)) = \int G(x, x'; \omega)\left(-\frac{1}{\varepsilon}\hat\rho(x', \omega), \mu\hat{\mathbf{j}}(x', \omega)\right)d^3x'.$$
(2.8)

We will exclusively use the whole-space Green function (2.7), symmetric with respect to the first and second argument.

The field strengths are found via the potential representation stated after (2.3). We define the bivector

$$g_{ik}(x, x'; \omega) := \left(\delta_{ik} + \frac{\partial_i\partial_k}{\varepsilon\mu\omega^2}\right)G(x, x'; \omega),$$
(2.9)

where both derivatives refer to x (although we may switch to the x' gradient if convenient, by substituting $\partial_k \to -\partial'_k$), and obtain

$$\hat{E}_i(x, \omega) = i\mu\omega\int g_{ik}(x, x'; \omega)\hat{j}_k(x', \omega)d^3x',$$
(2.10)

$$\hat{\mathbf{B}}(x, \omega) = -\mu\int\hat{\mathbf{j}}(x', \omega) \times \nabla G(x, x'; \omega)d^3x'.$$
(2.11)

The gradient ∇ refers to x, but we may replace $\nabla G \to -\nabla'G$, where the prime indicates x' differentiation. The d^3x' integration extends over the whole space. G satisfies the radiation condition $r(ik - \mathbf{n}\nabla)G = G$, and $G = O(1/r)$, with $r = |x - x'|$ and $\mathbf{n} = (x - x')/r$.

We consider a dipole current and the corresponding charge density,

$$\hat{\mathbf{j}}(x) = \mathbf{p}\delta(x - x_0), \quad \hat\rho(x) = \frac{1}{i\omega}(\mathbf{p}\nabla)\delta(x - x_0),$$
(2.12)

where $\mathbf{p}$ denotes an arbitrary constant vector (possibly depending on x_0), the charge density being obtained from the continuity equation, cf. after (2.3). The gradient in (2.12) refers to x, but we may substitute $\nabla \to -\nabla_0$, where ∇_0 is the x_0 gradient. The corresponding scalar and vector potentials are

$$\hat{A}_0(x, \omega) = \frac{i}{\varepsilon\omega}(\mathbf{p}\nabla)G(x, x_0; \omega), \quad \hat{\mathbf{A}}(x, \omega) = \mu G(x, x_0; \omega)\mathbf{p}.$$
(2.13)

The $\hat{\mathbf{E}}$ field generated by the dipole is $\hat{E}_i(x, \omega) = i\mu\omega g_{ik}p_k$, or

$$\hat{\mathbf{E}}(x, \omega) = i\mu\omega\left(\mathbf{p}G(x, x_0; \omega) + \frac{\mathbf{p}\nabla}{\varepsilon\mu\omega^2}\nabla G(x, x_0; \omega)\right),$$
(2.14)

and the magnetic counterpart reads

$$\hat{\mathbf{B}}(x, \omega) = -\mu\mathbf{p} \times \nabla G(x, x_0; \omega) = \mu\operatorname{rot}(\mathbf{p}G(x, x_0; \omega)).$$
(2.15)

(The dipole vector $\mathbf{p}$ is independent of x.) By making use of wave equation (2.6) for $G(x, x_0; \omega)$, we write the dipole field $\hat{\mathbf{E}}(x, \omega)$ in (2.14) as

$$\hat{\mathbf{E}}(x,\omega) = \frac{\mathrm{i}}{\varepsilon\omega}(\mu\varepsilon\omega^2 + \nabla\mathrm{div})(\mathbf{p}G)$$
$$= \frac{\mathrm{i}}{\varepsilon\omega}\left((\mathrm{rot\,rot} - m_\mathrm{t}^2)(\mathbf{p}G(x,x_0;\omega)) - \delta(x-x_0)\mathbf{p}\right). \qquad (2.16)$$

The substitutions $\nabla \rightarrow -\nabla_0$ and $\mathrm{rot} \rightarrow -\mathrm{rot}_0$ can be performed whenever convenient; the subscript zero denotes differentiation with respect to argument x_0 in the Green function. We write $\hat{\mathbf{E}}[\mathbf{p}]$ for the field (2.14) generated by a dipole $\mathbf{p}$, and analogously $\hat{\mathbf{B}}[\mathbf{p}]$ in (2.15). If $\mathbf{q}$ is another arbitrary constant dipole vector, then $\mathbf{q}\hat{\mathbf{E}}[\mathbf{p}] = \mathbf{p}\hat{\mathbf{E}}[\mathbf{q}]$, and the same holds true for $\hat{\mathbf{A}}[\mathbf{p}]$ in (2.13). We also note the anti-symmetry $\mathbf{q}\hat{\mathbf{B}}[\mathbf{p}] = -\mathbf{p}\hat{\mathbf{B}}[\mathbf{q}]$. If the dipole vectors $\mathbf{q}$ and $\mathbf{p}$ depend on x rather than x_0, these symmetries remain valid, provided that the gradients and rotors are replaced by the substitutions indicated after (2.16).

2.3. Kirchhoff representation of the tachyon potential and the field strengths

We denote the singular dipole current (2.12) and the dipole fields (2.13)–(2.16) by a subscript δ, e.g. $\hat{\mathbf{j}}_\delta$ and $\hat{\mathbf{E}}_\delta$, and consider a closed surface S around the dipole at x_0. An independent second set of fields, $\hat{\mathbf{E}}, \hat{\mathbf{B}}, \hat{\mathbf{A}}$, and $\hat{A}_0$, solves the free tachyonic Maxwell equations (2.2) inside the cavity defined by S. (These fields are supposed to be generated by a current distribution outside the enclosure S, but we will only be concerned with the fields in the interior.) We define the flux functional [24,25]

$$\mathbf{F}_\delta := \frac{1}{\mu}(\hat{\mathbf{E}} \times \hat{\mathbf{B}}_\delta - \hat{\mathbf{E}}_\delta \times \hat{\mathbf{B}}) + \frac{m_\mathrm{t}^2}{\mu}(\hat{A}_0\hat{\mathbf{A}}_\delta - \hat{A}_{\delta,0}\hat{\mathbf{A}}) \qquad (2.17)$$

(as suggested by analogy to the tachyonic Poynting vector, cf. after (3.3)), and apply the field equations as well as the potential representation of the field strengths to find $\mathrm{div}\mathbf{F}_\delta = -\hat{\mathbf{E}}\hat{\mathbf{j}}_\delta$ inside the cavity. The integration of the divergence over the cavity can be expressed as a surface integral, $\int_V \mathrm{div}\mathbf{F}_\delta \mathrm{d}^3x = -\int_S \mathbf{F}_\delta \mathbf{n}\mathrm{d}S'$, where $\mathbf{n}$ is the inward-pointing surface normal, and $\mathrm{d}\mathbf{S}' = \mathbf{n}\mathrm{d}S'$ the surface element. The volume integration of the δ current $\hat{\mathbf{j}}_\delta$ gives $-\hat{\mathbf{E}}(x_0,\omega)\mathbf{p}$, cf. (2.12). As for the surface integral, we substitute the identities

$$(\hat{\mathbf{E}} \times \hat{\mathbf{B}}_\delta[\mathbf{p}])\mathbf{n} = (\mathbf{n} \times \hat{\mathbf{E}})\hat{\mathbf{B}}_\delta[\mathbf{p}] = -\mathbf{p}\hat{\mathbf{B}}_\delta[\mathbf{n} \times \hat{\mathbf{E}}],$$
$$(\hat{\mathbf{E}}_\delta \times \hat{\mathbf{B}}[\mathbf{p}])\mathbf{n} = -(\mathbf{n} \times \hat{\mathbf{B}})\hat{\mathbf{E}}_\delta[\mathbf{p}] = -\mathbf{p}\hat{\mathbf{E}}_\delta[\mathbf{n} \times \hat{\mathbf{B}}]. \qquad (2.18)$$

Here, $\mathbf{n}(x')$, $\hat{\mathbf{E}}(x',\omega)$, etc., depend on a point x' on the boundary S. The Green's function $G(x',x_0;\omega)$ is symmetric with respect to an interchange of x' and x_0. It is also assumed that the substitutions $\nabla \rightarrow -\nabla_0$ and $\mathrm{rot} \rightarrow -\mathrm{rot}_0$ are performed in the dipole fields. Finally, we write x for x_0 (an arbitrary point inside the cavity), and drop the scalar multiplication with the arbitrary dipole vector $\mathbf{p}$, to obtain the surface-integral representation

$$\hat{\mathbf{E}}(x,\omega) = -\mathrm{rot}\int_S G(x,x';\omega)\hat{\mathbf{E}}(x',\omega) \times \mathrm{d}\mathbf{S}'$$
$$- \frac{\mathrm{i}}{\mu\varepsilon\omega}(\mathrm{rot\,rot} - m_\mathrm{t}^2)\int_S G(x,x';\omega)\hat{\mathbf{B}}(x',\omega) \times \mathrm{d}\mathbf{S}'$$
$$+ \frac{\mathrm{i}m_\mathrm{t}^2}{\mu\varepsilon\omega}\nabla\int_S G(x,x';\omega)\hat{\mathbf{A}}(x',\omega)\mathrm{d}\mathbf{S}'$$
$$+ m_\mathrm{t}^2\int_S G(x,x';\omega)\hat{A}_0(x',\omega)\mathrm{d}\mathbf{S}'. \qquad (2.19)$$

Here, $\mathrm{d}\mathbf{S}' = \mathbf{n}(x')\mathrm{d}S'$, where $\mathbf{n}(x')$ is the unit normal vector pointing into the interior of the cavity, and the integration $\mathrm{d}S'$ is over the closed boundary surface S. The field strengths and potentials satisfy the free field equations (2.2) and (2.3) (with $\varepsilon_0 = \varepsilon$ and $\mu_0 = \mu$) inside the cavity, that is, with zero current and charge density. $G(x,x';\omega)$ is the Green function (2.7), where x ranges inside the cavity, and the

integration is over the surface variable x'. The rotor and gradient refer to x. The potentials $\hat{\mathbf{A}}(x',\omega)$ and $\hat{A}_0(x',\omega)$ in the surface integrals can be replaced by field strengths (via substitution of the field equations), and the operator $(\mathrm{rot\,rot} - m_\mathrm{t}^2)$ by $(\mu\varepsilon\omega^2 + \nabla\mathrm{div})$, cf. (2.16).

We use $\hat{A}_0 = -(1/m_\mathrm{t}^2)\mathrm{div}\hat{\mathbf{E}}$ to obtain the Kirchhoff identity for the scalar potential,

$$\hat{A}_0(x,\omega) = -\frac{\mathrm{i}}{\mu\varepsilon\omega}\mathrm{div}\int_S G(x,x';\omega)\hat{\mathbf{B}}(x',\omega) \times \mathrm{d}\mathbf{S}'$$
$$- \mathrm{div}\int_S G(x,x';\omega)\hat{A}_0(x',\omega)\mathrm{d}\mathbf{S}'$$
$$+ \frac{\mathrm{i}k^2}{\mu\varepsilon\omega}\int_S G(x,x';\omega)\hat{\mathbf{A}}(x',\omega)\mathrm{d}\mathbf{S}'. \qquad (2.20)$$

The differential operators rot, div, and ∇ refer to variable x in the Green's function. The Kirchhoff identity for the vector potential is found by means of $\mathrm{i}\omega\hat{\mathbf{A}} = \hat{\mathbf{E}} - \nabla\hat{A}_0$,

$$\hat{\mathbf{A}}(x,\omega) = \frac{\mathrm{i}}{\omega}\mathrm{rot}\int_S G(x,x';\omega)\hat{\mathbf{E}}(x',\omega) \times \mathrm{d}\mathbf{S}'$$
$$- \int_S G(x,x';\omega)\hat{\mathbf{B}}(x',\omega) \times \mathrm{d}\mathbf{S}'$$
$$- \nabla\int_S G(x,x';\omega)\hat{\mathbf{A}}(x',\omega)\mathrm{d}\mathbf{S}'$$
$$- \frac{\mathrm{i}}{\omega}(\mathrm{rot\,rot} - \mu\varepsilon\omega^2)\int_S G(x,x';\omega)\hat{A}_0(x',\omega)\mathrm{d}\mathbf{S}', \qquad (2.21)$$

where we may substitute $(m_\mathrm{t}^2 + \nabla\mathrm{div})$ for $(\mathrm{rot\,rot} - \mu\varepsilon\omega^2)$. The analogous surface-integral representation of the magnetic field is obtained via $\hat{\mathbf{B}} = \mathrm{rot}\hat{\mathbf{A}}$,

$$\hat{\mathbf{B}}(x,\omega) = \frac{\mathrm{i}}{\omega}\mathrm{rot\,rot}\int_S G(x,x';\omega)\hat{\mathbf{E}}(x',\omega) \times \mathrm{d}\mathbf{S}'$$
$$- \mathrm{rot}\int_S G(x,x';\omega)\hat{\mathbf{B}}(x',\omega) \times \mathrm{d}\mathbf{S}'$$
$$- \frac{\mathrm{i}}{\omega}m_\mathrm{t}^2\mathrm{rot}\int_S G(x,x';\omega)\hat{A}_0(x',\omega)\mathrm{d}\mathbf{S}', \qquad (2.22)$$

where $\mathrm{rot\,rot} = (k^2 + \nabla\mathrm{div})$. These identities follow from the electric field strength (2.19), by applying the field equations or potential representation, without actually solving differential equations. We also note that the Green function in these identities is the whole-space Green function (2.7), and is not required to satisfy any particular boundary conditions on the closed surface S, for technical simplicity. Therefore, these identities are only valid for solutions of the field equations, so that the boundary values cannot be arbitrarily prescribed. In the next section, however, we will prescribe boundary conditions, and convince ourselves that the fields calculated by means of the above Kirchhoff identities are asymptotic solutions of the free tachyonic Maxwell equations (2.2). This is in fact the practical use of these identities: Even though they will not give exact solutions for arbitrary boundary values, the resulting fields may well be approximate solutions in the far-field regime, which has to be checked on a case-by-case basis, by substitution into the field equations.

3. Fraunhofer diffraction of superluminal radiation at a plane aperture

3.1. Tachyonic energy flux

As in Section 2.2, we put $\varepsilon_0 = \varepsilon$ and $\mu_0 = \mu$. When studying diffraction in the far-field limit [26,27], it suffices to use the dipole approximation $|x - x'| \sim r(1 - \mathbf{n}x'/r)$, where $r = |\mathbf{x}|$ and $\mathbf{n} = \mathbf{x}/r$, so that (for large r and $|\mathbf{x}'| = O(1)$)

$$G(x,x';\omega) \sim \frac{1}{4\pi r}\exp(\mathrm{i}k(\omega)(r - \mathbf{n}x')), \quad \nabla G \sim \mathrm{i}k\mathbf{n}G. \qquad (3.1)$$

We consider an enclosure defined by a hemisphere in the upper half-space. The radius of this hemisphere will ultimately be expanded to infinity, so that the enclosure is just the upper half-space, bounded by the (x,y) plane with inward-pointing normal vector $\mathbf{e}_3 = (0,0,1)$. We consider an aperture A in the (x,y) plane, centered at the coordinate origin, and an incoming plane-wave propagating in the lower half-space towards the aperture. The wave diffracted through the aperture into the upper half-space is obtained from the Kirchhoff identities Eq. (2.19)–(2.22), where we identify the (x,y) plane with the boundary surface S. At the perfectly conducting boundary, the complement of the aperture, we assume zero potentials and field strengths, and in the aperture A we use the incoming plane wave as boundary value. The mentioned hemisphere (defining a finite cavity as an intermediate step) does not give a contribution to the surface integrals when expanded to infinity, as the Green's function satisfies the radiation condition, cf. after (2.11).

To find the energy flux carried by polarized superluminal modes incident upon the aperture, we use a plane-wave ansatz in the tachyonic Maxwell equations (2.2) (with vanishing charge and current, as well as $\varepsilon_0 = \varepsilon$ and $\mu_0 = \mu$), $\hat{\mathbf{A}}(\mathbf{x}, \omega) = \mathbf{A}(\mathbf{k})e^{i\mathbf{k}\mathbf{x}}$, and analogously for the scalar potential and the field strengths. Here, $\mathbf{k} = k(\omega)\mathbf{k}_0$, where k is the wave number in the Green function (2.7), and $\mathbf{k}_0$ a constant unit vector. The transversality condition is $\hat{\mathbf{A}}\mathbf{k}_0 = 0$, and the set of transversal modes reads

$$\mathbf{k}_0\hat{\mathbf{A}}^T = 0, \quad \hat{A}_0^T = 0, \quad \hat{\mathbf{E}}^T = i\omega\hat{\mathbf{A}}^T, \quad \hat{\mathbf{B}}^T = ik(\omega)\mathbf{k}_0 \times \hat{\mathbf{A}}^T. \quad (3.2)$$

If the product $\hat{\mathbf{A}}\mathbf{k}_0$ does not vanish, then the modes are longitudinal,

$$\hat{\mathbf{A}}^L = (\hat{\mathbf{A}}^L\mathbf{k}_0)\mathbf{k}_0, \quad \hat{A}_0^L = -\frac{k(\omega)}{\varepsilon\mu\omega}\mathbf{k}_0\hat{\mathbf{A}}^L, \quad \hat{\mathbf{E}}^L = \frac{m_t^2}{i\varepsilon\mu\omega}\hat{\mathbf{A}}^L, \quad \hat{\mathbf{B}}^L = 0. \quad (3.3)$$

We substitute these plane-wave solutions into the tachyonic Poynting vector $\mathbf{S} = \mathbf{E} \times \mathbf{H} + m_t^2 A_0 \mathbf{C}$ [28], and perform a time average, to obtain the transversal and longitudinal components of the energy flux,

$$\langle \mathbf{S}^T \rangle = \frac{2k}{\mu}\omega|\hat{\mathbf{A}}^T|^2\mathbf{k}_0, \quad \langle \mathbf{S}^L \rangle = \frac{2k}{\mu^2\varepsilon}\frac{m_t^2}{\omega}|\hat{\mathbf{A}}^L|^2\mathbf{k}_0. \quad (3.4)$$

Here, real permeabilities and a positive wave number $k(\omega)$ are implied.

3.2. Polarized superluminal modes: conversion of transversal into longitudinal tachyons by diffraction

We consider an incident transversal plane wave, propagating in the lower half-space toward the aperture A in the (x,y) plane. The Fourier amplitude of the vector potential is $\hat{\mathbf{A}}_{in}^T = \mathbf{A}_{in}^T e^{i\mathbf{k}\mathbf{x}}$, $\mathbf{A}_{in}^T \mathbf{k}_0 = 0$, cf. (3.2). By making use of the Kirchhoff identity (2.19) and the limit procedure outlined after (3.1), we find the leading asymptotic order ($r \to \infty$, Fraunhofer regime [29]) of the diffracted wave in the upper half-space as

$$\hat{\mathbf{E}}_{out}(x, \omega) \sim \omega k M \frac{e^{ikr}}{4\pi r}((\mathbf{e}_3\mathbf{n})\mathbf{A}_{in}^T - (\mathbf{A}_{in}^T\mathbf{n})\mathbf{e}_3 + (\mathbf{e}_3\mathbf{k}_0)\mathbf{A}_{in}^T$$
$$- (\mathbf{e}_3\mathbf{A}_{in}^T)\mathbf{k}_0 + (\mathbf{e}_3\mathbf{A}_{in}^T)(\mathbf{k}_0\mathbf{n})\mathbf{n} - (\mathbf{e}_3\mathbf{k}_0)(\mathbf{A}_{in}^T\mathbf{n})\mathbf{n})$$
$$+ \frac{m_t^2 k M}{\mu\varepsilon\omega}\frac{e^{ikr}}{4\pi r}((\mathbf{e}_3\mathbf{A}_{in}^T)(\mathbf{k}_0\mathbf{n})\mathbf{n} - (\mathbf{e}_3\mathbf{k}_0)(\mathbf{A}_{in}^T\mathbf{n})\mathbf{n}$$
$$- (\mathbf{e}_3\mathbf{A}_{in}^T)\mathbf{n}). \quad (3.5)$$

The notation is explained in Section 3.1; the modulation factor is

$$M := \int_A \exp(ik(\mathbf{k}_0 - \mathbf{n})\mathbf{x}')dx'dy', \quad (3.6)$$

where $\mathbf{x}' = (x', y', z' = 0)$ [20]. The scalar potential reads, cf. (2.20),

$$\hat{A}_{0,out}(x, \omega) \sim \frac{ik^2 M}{\mu\varepsilon\omega}\frac{e^{ikr}}{4\pi r}((\mathbf{e}_3\mathbf{A}_{in}^T) - (\mathbf{n}\mathbf{k}_0)(\mathbf{e}_3\mathbf{A}_{in}^T) + (\mathbf{n}\mathbf{A}_{in}^T)(\mathbf{e}_3\mathbf{k}_0)), \quad (3.7)$$

and the vector potential, cf. (2.21),

$$\hat{\mathbf{A}}_{out}(x, \omega) \sim -ikM\frac{e^{ikr}}{4\pi r}((\mathbf{e}_3\mathbf{n})\mathbf{A}_{in}^T - (\mathbf{A}_{in}^T\mathbf{n})\mathbf{e}_3 + (\mathbf{e}_3\mathbf{k}_0)\mathbf{A}_{in}^T$$
$$- (\mathbf{e}_3\mathbf{A}_{in}^T)\mathbf{k}_0 + (\mathbf{e}_3\mathbf{A}_{in}^T)\mathbf{n}). \quad (3.8)$$

The magnetic field strength is found as, cf. (2.22),

$$\hat{\mathbf{B}}_{out}(x, \omega) \sim k^2 M\frac{e^{ikr}}{4\pi r}(\mathbf{e}_3 \times \mathbf{A}_{in}^T - ((\mathbf{e}_3 \times \mathbf{A}_{in}^T)\mathbf{n})\mathbf{n}$$
$$+ (\mathbf{n} \times \mathbf{A}_{in}^T)(\mathbf{e}_3\mathbf{k}_0) - (\mathbf{n} \times \mathbf{k}_0)(\mathbf{e}_3\mathbf{A}_{in}^T)). \quad (3.9)$$

When calculating the intensity of the diffracted superluminal flux, we need the transversal and longitudinal projections of the vector potential, that is $\varepsilon_j\hat{\mathbf{A}}_{out}$ and $\mathbf{n}\hat{\mathbf{A}}_{out}$, respectively. Here, ε_j and $\mathbf{n} = \mathbf{x}/r$ constitute the orthonormal triad defining the outgoing linear polarizations, $\mathbf{n}$ being the unit wave vector of the outgoing spherical wave. The incident transversal wave is linearly polarized, $\mathbf{A}_{in}^T = \varepsilon_{0,i}A_{in}^T$; the transversal linear polarization vectors $\varepsilon_{0,1}$ and $\varepsilon_{0,2}$ of the incoming wave are real and define with its unit wave vector $\mathbf{k}_0$ an orthonormal triad, so that $\mathbf{k}_0 = \varepsilon_{0,1} \times \varepsilon_{0,2}$ cyclically.

As for the outgoing transversal polarization vectors ε_j of the diffracted wave in the upper half-space, we choose two real vectors $\varepsilon_{1,2}$ orthogonal to $\mathbf{n}$, so that ε_1 lies in the plane generated by $\mathbf{n}$ and the incident unit wave vector $\mathbf{k}_0$,

$$\varepsilon_2 = \frac{\mathbf{n} \times \mathbf{k}_0}{|\mathbf{n} \times \mathbf{k}_0|}, \quad \varepsilon_1 = \varepsilon_2 \times \mathbf{n} = \frac{\mathbf{k}_0 - \mathbf{n}(\mathbf{n}\mathbf{k}_0)}{|\mathbf{n} \times \mathbf{k}_0|}. \quad (3.10)$$

We note $\mathbf{n} = \varepsilon_1 \times \varepsilon_2$, and $|\mathbf{n} \times \mathbf{k}_0|^2 = 1 - (\mathbf{n}\mathbf{k}_0)^2$. The scalar products of the transversal polarization vectors of the incoming and outgoing waves read

$$\varepsilon_2\varepsilon_{0,1} = \frac{\mathbf{n}\varepsilon_{0,2}}{|\mathbf{n} \times \mathbf{k}_0|}, \quad \varepsilon_2\varepsilon_{0,2} = -\frac{\mathbf{n}\varepsilon_{0,1}}{|\mathbf{n} \times \mathbf{k}_0|},$$
$$\varepsilon_1\varepsilon_{0,i} = -\frac{(\mathbf{n}\varepsilon_{0,i})(\mathbf{n}\mathbf{k}_0)}{|\mathbf{n} \times \mathbf{k}_0|}, \quad \sum_{i,k}|\varepsilon_i\varepsilon_{0,k}|^2 = 1 + (\mathbf{n}\mathbf{k}_0)^2. \quad (3.11)$$

The longitudinal polarization vectors of the in- and outgoing waves are the unit wave vectors $\mathbf{k}_0$ and $\mathbf{n}$, respectively. The angular parametrization of these products is done with polar coordinates in the coordinate frame defined by the right-handed triad $\varepsilon_{0,1}$, $\varepsilon_{0,2}$, and $\mathbf{k}_0$ of the incoming wave. Thus, $\mathbf{n}\mathbf{k}_0 = \cos\theta$, $\mathbf{n}\varepsilon_{0,1} = \cos\varphi \sin\theta$, and $\mathbf{n}\varepsilon_{0,2} = \sin\varphi\sin\theta$, and $d\Omega = \sin\theta d\theta d\varphi$ is the solid angle element. Accordingly, $|\mathbf{n} \times \mathbf{k}_0| = \sin\theta$, and

$$\varepsilon_1\varepsilon_{0,1} = -\cos\theta\cos\varphi, \quad \varepsilon_1\varepsilon_{0,2} = -\cos\theta\sin\varphi,$$
$$\varepsilon_2\varepsilon_{0,1} = \sin\varphi, \quad \varepsilon_2\varepsilon_{0,2} = -\cos\varphi. \quad (3.12)$$

The $\mathbf{e}_3$ projection of the outgoing polarization triad is related to the $\mathbf{e}_3$ projection of the incoming triad as

$$\mathbf{n}\mathbf{e}_3 = \varepsilon_{0,1}\mathbf{e}_3 \sin\theta\cos\varphi + \varepsilon_{0,2}\mathbf{e}_3 \sin\theta\sin\varphi + \mathbf{k}_0\mathbf{e}_3\cos\theta,$$
$$\varepsilon_1\mathbf{e}_3 = -\varepsilon_{0,1}\mathbf{e}_3\cos\theta\cos\varphi - \varepsilon_{0,2}\mathbf{e}_3\cos\theta\sin\varphi + \mathbf{k}_0\mathbf{e}_3\sin\theta, \quad (3.13)$$
$$\varepsilon_2\mathbf{e}_3 = \varepsilon_{0,1}\mathbf{e}_3\sin\varphi - \varepsilon_{0,2}\mathbf{e}_3\cos\varphi.$$

The angular parametrization of the polarized components of the diffracted wave (3.8) can readily be performed by substitution of these scalar products. The transversal ε_j projections of (3.8) read

$$\varepsilon_j\hat{\mathbf{A}}_{out}(x, \omega, \varepsilon_{0,i}) \sim -ikMA_{in}^T\frac{e^{ikr}}{4\pi r}((\varepsilon_{0,i}\varepsilon_j)(\mathbf{e}_3\mathbf{n} + \mathbf{e}_3\mathbf{k}_0)$$
$$- (\varepsilon_{0,i}\mathbf{n})(\mathbf{e}_3\varepsilon_j) - (\varepsilon_{0,i}\varepsilon_3)(\mathbf{k}_0\varepsilon_j)). \quad (3.14)$$

The polarization vector of the incident wave, $\mathbf{A}_{in}^T = \varepsilon_{0,i}A_{in}^T$, is indicated as argument. The longitudinal projection of the outgoing wave (3.8) is

$$\mathbf{n}\hat{\mathbf{A}}_{\text{out}}(x,\omega,\boldsymbol{\varepsilon}_{0,i}) \sim -ikMA_{\text{in}}^{\text{T}}\frac{e^{ikr}}{4\pi r}((\boldsymbol{\varepsilon}_{0,i}\mathbf{n})(\mathbf{e}_3\mathbf{k}_0) + (\boldsymbol{\varepsilon}_{0,i}\mathbf{e}_3)(1 - \mathbf{k}_0\mathbf{n})). \tag{3.15}$$

We consider the special case where the incoming wave vector is normal to the plane of incidence. As $\mathbf{k}_0 = \mathbf{e}_3$, the angular parametrization of the cross sections greatly simplifies, but the above parametrization of the polarization triads can be used for any other incident wave vector as well. On performing the average over the initial transversal polarizations and a summation over the transversal outgoing polarizations, we obtain, cf. (3.14),

$$|\hat{\mathbf{A}}|_{\text{T}\to\text{T}}^2 := \frac{1}{2}\sum_{i,j}|\boldsymbol{\varepsilon}_j\hat{\mathbf{A}}_{\text{out}}(x,\omega,\boldsymbol{\varepsilon}_{0,i})|^2 \sim k^2\frac{|M|^2\left|A_{\text{in}}^{\text{T}}\right|^2}{(4\pi r)^2}(1 + \cos\theta)^2, \tag{3.16}$$

where we used

$$\sum_{i,j}((\boldsymbol{\varepsilon}_{0,i}\boldsymbol{\varepsilon}_j)(1 + \mathbf{k}_0\mathbf{n}) - (\boldsymbol{\varepsilon}_{0,i}\mathbf{n})(\mathbf{k}_0\boldsymbol{\varepsilon}_j))^2 = 2(1 + \cos\theta)^2. \tag{3.17}$$

The angular parametrization of the longitudinal outgoing component (3.15) at normal incidence $\mathbf{k}_0 = \mathbf{e}_3$ reads

$$|\hat{\mathbf{A}}|_{\text{T}\to\text{L}}^2 := \frac{1}{2}\sum_i|\mathbf{n}\hat{\mathbf{A}}_{\text{out}}(x,\omega,\boldsymbol{\varepsilon}_{0,i})|^2 \sim \frac{k^2}{2}\frac{|M|^2\left|A_{\text{in}}^{\text{T}}\right|^2}{(4\pi r)^2}\sin^2\theta. \tag{3.18}$$

These averages suffice to calculate the intensity ratios determining the conversion efficiency, cf. (3.25).

In the far-field limit, the outgoing spherical waves are structured as [28]

$$\hat{\mathbf{A}}_{\text{out}}^{\text{T,L}}(x,\omega) \sim \frac{1}{4\pi r}\exp(ik(\omega)r)\hat{\mathbf{J}}^{\text{T,L}}(\mathbf{x},\omega) + O\left(\frac{1}{r^2}\right), \tag{3.19}$$

where $\mathbf{n}\hat{\mathbf{J}}^{\text{T}} = 0$ and $\hat{\mathbf{J}}^{\text{L}} = \mathbf{n}(\mathbf{n}\hat{\mathbf{J}}^{\text{L}})$. The amplitudes $\hat{\mathbf{J}}^{\text{T,L}}$ are slowly varying in the space coordinates, so that we find the leading asymptotic order of the tachyonic field strengths and the scalar potential as

$$\begin{aligned}
&\hat{\mathbf{E}}_{\text{out}}^{\text{T}} \sim i\omega\hat{\mathbf{A}}_{\text{out}}^{\text{T}}, \quad \hat{\mathbf{B}}_{\text{out}}^{\text{T}} \sim ik\mathbf{n}\times\hat{\mathbf{A}}_{\text{out}}^{\text{T}}, \quad \hat{A}_{0,\text{out}}^{\text{T}} \sim O(1/r^2), \\
&\hat{\mathbf{E}}_{\text{out}}^{\text{L}} \sim \frac{m_t^2}{i\omega\varepsilon\mu}\hat{\mathbf{A}}_{\text{out}}^{\text{L}}, \quad \hat{\mathbf{B}}_{\text{out}}^{\text{L}} \sim O\left(\frac{1}{r^2}\right), \quad \hat{A}_{0,\text{out}}^{\text{L}} \sim -\frac{k}{\omega\varepsilon\mu}\mathbf{n}\hat{\mathbf{A}}_{\text{out}}^{\text{L}}.
\end{aligned} \tag{3.20}$$

The transversal component $\hat{\mathbf{A}}_{\text{out}}^{\text{T}}$ is an arbitrary complex linear combination of the two linear polarization components $\boldsymbol{\varepsilon}_j(\boldsymbol{\varepsilon}_j\hat{\mathbf{A}}_{\text{out}})$, cf. (3.14). The plane-wave counterpart to (3.20) is stated in (3.2) and (3.3). The time-averaged superluminal flux vectors $\langle\mathbf{S}^{\text{T,L}}\rangle$ can be assembled with these asymptotic spherical waves as done in (3.4) for plane waves. The transversal and longitudinal components of the diffracted energy flux are

$$\left\langle\mathbf{S}_{\text{out}}^{\text{T}}\right\rangle_{ij} = \frac{2k}{\mu}\omega|\boldsymbol{\varepsilon}_j\hat{\mathbf{A}}_{\text{out}}(\boldsymbol{\varepsilon}_{0,i})|^2\mathbf{n}, \quad \left\langle\mathbf{S}_{\text{out}}^{\text{L}}\right\rangle_i = \frac{2k}{\mu^2\varepsilon}\frac{m_t^2}{\omega}|\mathbf{n}\hat{\mathbf{A}}_{\text{out}}(\boldsymbol{\varepsilon}_{0,i})|^2\mathbf{n}, \tag{3.21}$$

where we substitute the amplitudes (3.14) and (3.15). The subscripts i and j refer to the respective incoming and outgoing transversal polarization states. These averages are obtained from the asymptotic time-averaged Poynting vectors, cf. after (3.3),

$$\langle\mathbf{S}^{\text{T}}\rangle \sim (1/\mu)\hat{\mathbf{E}}^{\text{T}}\times\hat{\mathbf{B}}^{\text{T}*} + \text{c.c.}, \quad \langle\mathbf{S}^{\text{L}}\rangle \sim -(m_t^2/\mu)\hat{A}_0^{\text{L}}\hat{\mathbf{A}}^{\text{L}*} + \text{c.c.} \tag{3.22}$$

The diffracted flux components are to be compared to the flux carried by the incident transversal plane wave, cf. (3.4),

$$\left\langle\mathbf{S}_{\text{in}}^{\text{T}}\right\rangle = \frac{2k}{\mu}\omega\left|A_{\text{in}}^{\text{T}}\right|^2\mathbf{k}_0. \tag{3.23}$$

As for the outgoing flux vectors (3.21), we perform the same average/summation over the transversal polarizations as done in

(3.16) and (3.18). The ratio of the outgoing flux transversally or longitudinally diffracted into the solid angle element $d\Omega$ and the transversal flux incident upon the aperture area is found as

$$d\sigma_{\text{T}\to\text{T}} := \frac{\left\langle\mathbf{S}_{\text{out}}^{\text{T}}\right\rangle\mathbf{n}r^2d\Omega}{\left\langle\mathbf{S}_{\text{in}}^{\text{T}}\right\rangle\mathbf{e}_3\,\text{area}(A)}, \quad d\sigma_{\text{T}\to\text{L}} := \frac{\left\langle\mathbf{S}_{\text{out}}^{\text{L}}\right\rangle\mathbf{n}r^2d\Omega}{\left\langle\mathbf{S}_{\text{in}}^{\text{T}}\right\rangle\mathbf{e}_3\,\text{area}(A)}. \tag{3.24}$$

These are dimensionless intensity ratios, cross sections divided by the aperture area. On substituting the averages (3.16) and (3.18), we find the intensity ratios for the diffraction of transversal radiation,

$$d\sigma_{\text{T}\to\text{T}} = \frac{\left|\hat{\mathbf{A}}\right|_{\text{T}\to\text{T}}^2 r^2d\Omega}{\left|A_{\text{in}}^{\text{T}}\right|^2\text{area}(A)}, \quad d\sigma_{\text{T}\to\text{L}} = \frac{m_t^2}{\mu\varepsilon\omega^2}\frac{\left|\hat{\mathbf{A}}\right|_{\text{T}\to\text{L}}^2 r^2d\Omega}{\left|A_{\text{in}}^{\text{T}}\right|^2\text{area}(A)}. \tag{3.25}$$

Diffraction of transversal wave fields generates longitudinal modes, the conversion efficiency being determined by the ratio $d\sigma_{\text{T}\to\text{L}}/(d\sigma_{\text{T}\to\text{T}} + d\sigma_{\text{T}\to\text{L}})$.

3.3. Intensity ratios for the conversion of longitudinal into transversal radiation

We consider an incident longitudinal plane wave, $\hat{\mathbf{A}}_{\text{in}}^{\text{L}} = \mathbf{A}_{\text{in}}^{\text{L}}e^{i\mathbf{kx}}, \mathbf{A}_{\text{in}}^{\text{L}} = \mathbf{k}_0A_{\text{in}}^{\text{L}}$, cf. (3.3), and proceed analogously to the transversal case in Section 3.2. Employing the surface integrals (2.19)–(2.22), we find the diffracted electric field strength in the Fraunhofer regime,

$$\hat{\mathbf{E}}_{\text{out}}(x,\omega) \sim -\frac{m_t^2kM}{\mu\varepsilon\omega}\frac{e^{ikr}}{4\pi r}((\mathbf{e}_3\mathbf{n})\mathbf{A}_{\text{in}}^{\text{L}} - (\mathbf{A}_{\text{in}}^{\text{L}}\mathbf{n})\mathbf{e}_3 + (\mathbf{e}_3\mathbf{A}_{\text{in}}^{\text{L}})\mathbf{n} + (\mathbf{k}_0\mathbf{A}_{\text{in}}^{\text{L}})\mathbf{e}_3), \tag{3.26}$$

the scalar potential,

$$\hat{A}_{0,\text{out}}(x,\omega) \sim \frac{ik^2M}{\mu\varepsilon\omega}\frac{e^{ikr}}{4\pi r}((\mathbf{e}_3\mathbf{A}_{\text{in}}^{\text{L}}) + (\mathbf{k}_0\mathbf{A}_{\text{in}}^{\text{L}})(\mathbf{e}_3\mathbf{n})), \tag{3.27}$$

the vector potential,

$$\begin{aligned}
\hat{\mathbf{A}}_{\text{out}}(x,\omega) \sim &-ikM\frac{e^{ikr}}{4\pi r}((\mathbf{e}_3\mathbf{A}_{\text{in}}^{\text{L}})\mathbf{n} + (\mathbf{k}_0\mathbf{A}_{\text{in}}^{\text{L}})(\mathbf{e}_3\mathbf{n})\mathbf{n}) \\
&+ i\frac{m_t^2kM}{\mu\varepsilon\omega^2}\frac{e^{ikr}}{4\pi r}((\mathbf{e}_3\mathbf{n})\mathbf{A}_{\text{in}}^{\text{L}} - (\mathbf{A}_{\text{in}}^{\text{L}}\mathbf{n})\mathbf{e}_3 \\
&+ (\mathbf{k}_0\mathbf{A}_{\text{in}}^{\text{L}})\mathbf{e}_3 - (\mathbf{k}_0\mathbf{A}_{\text{in}}^{\text{L}})(\mathbf{e}_3\mathbf{n})\mathbf{n}),
\end{aligned} \tag{3.28}$$

and the magnetic field strength

$$\hat{\mathbf{B}}_{\text{out}}(x,\omega) \sim -\frac{m_t^2k^2M}{\mu\varepsilon\omega^2}\frac{e^{ikr}}{4\pi r}(\mathbf{e}_3\times\mathbf{A}_{\text{in}}^{\text{L}} - ((\mathbf{e}_3\times\mathbf{A}_{\text{in}}^{\text{L}})\mathbf{n})\mathbf{n} + (\mathbf{n}\times\mathbf{e}_3)(\mathbf{k}_0\mathbf{A}_{\text{in}}^{\text{L}})). \tag{3.29}$$

The transversal polarization components of the diffracted vector potential $\hat{\mathbf{A}}_{\text{out}}$ in (3.28) read, cf. (3.14),

$$\boldsymbol{\varepsilon}_j\hat{\mathbf{A}}_{\text{out}}(x,\omega,\mathbf{k}_0) \sim i\frac{m_t^2kMA_{\text{in}}^{\text{L}}}{\mu\varepsilon\omega^2}\frac{e^{ikr}}{4\pi r}((\mathbf{e}_3\mathbf{n})(\mathbf{k}_0\boldsymbol{\varepsilon}_j) + (\mathbf{e}_3\boldsymbol{\varepsilon}_j)(1 - \mathbf{k}_0\mathbf{n})), \tag{3.30}$$

where we explicitly indicate the incoming longitudinal polarization $\mathbf{k}_0$ as argument. The outgoing longitudinal component is

$$\mathbf{n}\hat{\mathbf{A}}_{\text{out}}(x,\omega,\mathbf{k}_0) \sim -ikMA_{\text{in}}^{\text{L}}\frac{e^{ikr}}{4\pi r}(\mathbf{e}_3\mathbf{k}_0 + \mathbf{e}_3\mathbf{n}). \tag{3.31}$$

The angular parametrization is explained in (3.11)–(3.13). At normal incidence $\mathbf{k}_0 = \mathbf{e}_3$, we find $\boldsymbol{\varepsilon}_2\hat{\mathbf{A}}_{\text{out}} = 0$ and, cf. (3.16),

$$\left|\hat{\mathbf{A}}\right|_{\text{L}\to\text{T}}^2 := |\boldsymbol{\varepsilon}_1\hat{\mathbf{A}}_{\text{out}}(x,\omega,\mathbf{k}_0)|^2 \sim \frac{m_t^4k^2}{\mu^2\varepsilon^2\omega^4}\frac{|M|^2\left|A_{\text{in}}^{\text{L}}\right|^2}{(4\pi r)^2}\sin^2\theta. \tag{3.32}$$

The transversally diffracted radiation is thus linearly polarized. The squared longitudinal component (3.31) is parametrized as, cf. (3.18),

$$\left|\hat{\mathbf{A}}\right|_{\mathrm{L}\to\mathrm{L}}^{2} := |\mathbf{n}\hat{\mathbf{A}}_{\mathrm{out}}(x,\omega,\mathbf{k}_{0})|^{2} \sim k^{2}\frac{|M|^{2}\left|A_{\mathrm{in}}^{\mathrm{L}}\right|^{2}}{(4\pi r)^{2}}(1+\cos\theta)^{2}. \tag{3.33}$$

Regarding the energy flux, we note the polarized outgoing Poynting vectors, cf. (3.21),

$$\left\langle\mathbf{S}_{\mathrm{out}}^{\mathrm{T}}\right\rangle_{j} = \frac{2k}{\mu}\omega|\varepsilon_{j}\hat{\mathbf{A}}_{\mathrm{out}}(\mathbf{k}_{0})|^{2}\mathbf{n}, \quad \left\langle\mathbf{S}_{\mathrm{out}}^{\mathrm{L}}\right\rangle = \frac{2k}{\mu^{2}\varepsilon}\frac{m_{\mathrm{t}}^{2}}{\omega}|\mathbf{n}\hat{\mathbf{A}}_{\mathrm{out}}(\mathbf{k}_{0})|^{2}\mathbf{n}, \tag{3.34}$$

the incoming longitudinal flux vector, cf. (3.4),

$$\left\langle\mathbf{S}_{\mathrm{in}}^{\mathrm{L}}\right\rangle = \frac{2k}{\mu^{2}\varepsilon}\frac{m_{\mathrm{t}}^{2}}{\omega}\left|A_{\mathrm{in}}^{\mathrm{L}}\right|^{2}\mathbf{k}_{0}, \tag{3.35}$$

and the intensity ratios for the conversion of longitudinal radiation, cf. (3.24),

$$\mathrm{d}\sigma_{\mathrm{L}\to\mathrm{T}} := \frac{\left\langle\mathbf{S}_{\mathrm{out}}^{\mathrm{T}}\right\rangle\mathbf{n}r^{2}\mathrm{d}\Omega}{\left\langle\mathbf{S}_{\mathrm{in}}^{\mathrm{L}}\right\rangle\mathbf{e}_{3}\mathrm{area}(A)}, \quad \mathrm{d}\sigma_{\mathrm{L}\to\mathrm{L}} := \frac{\left\langle\mathbf{S}_{\mathrm{out}}^{\mathrm{L}}\right\rangle\mathbf{n}r^{2}\mathrm{d}\Omega}{\left\langle\mathbf{S}_{\mathrm{in}}^{\mathrm{L}}\right\rangle\mathbf{e}_{3}\mathrm{area}(A)}. \tag{3.36}$$

The conversion efficiency of longitudinal radiation into linearly polarized transversal tachyons is thus determined by the ratios, cf. (3.25),

$$\mathrm{d}\sigma_{\mathrm{L}\to\mathrm{T}} = \frac{\mu\varepsilon\omega^{2}}{m_{\mathrm{t}}^{2}}\frac{\left|\hat{\mathbf{A}}\right|_{\mathrm{L}\to\mathrm{T}}^{2}r^{2}\mathrm{d}\Omega}{\left|A_{\mathrm{in}}^{\mathrm{L}}\right|^{2}\mathrm{area}(A)}, \quad \mathrm{d}\sigma_{\mathrm{L}\to\mathrm{L}} = \frac{\left|\hat{\mathbf{A}}\right|_{\mathrm{L}\to\mathrm{L}}^{2}r^{2}\mathrm{d}\Omega}{\left|A_{\mathrm{in}}^{\mathrm{L}}\right|^{2}\mathrm{area}(A)}, \tag{3.37}$$

with the squared amplitude projections (3.32) and (3.33) substituted.

4. Tachyonic Bragg scattering

4.1. Diffraction gratings: negative mass-square and Bragg condition

We start with a grating defined as an array of $2N+1$ slits parallel to the $\mathbf{e}_{2}$ axis (y coordinate). The slits are rectangles of (large) height $2b$ and width $2a$. The x coordinate along $\mathbf{e}_{1}$ ranges in equidistantly spaced intervals $[nd-a,nd+a]$, where $n=-N,\dots,0,\dots,N$, and $d>2a$. The y coordinate of this grating aperture ranges in $[-b,b]$, and the modulation function (3.6) factorizes accordingly as

$$M = \int_{-b}^{b}\exp(\mathrm{i}kq_{2}y')\mathrm{d}y'\sum_{n=-N}^{N}\int_{nd-a}^{nd+a}\exp(\mathrm{i}kq_{1}x')\mathrm{d}x', \tag{4.1}$$

where $q_{1,2} := (\mathbf{k}_{0}-\mathbf{n})\mathbf{e}_{1,2}$. We note the identity

$$\sum_{n=-N}^{N}\exp(2\mathrm{i}\eta n) = \frac{\sin(\eta(2N+1))}{\sin\eta}, \tag{4.2}$$

as well as two limit definitions of the delta function, $\delta_{(1),(2)}(x,b\to\infty)=\delta(x)$, where

$$\delta_{(1)}(x,b) := \frac{1}{2\pi}\int_{-b}^{b}\mathrm{e}^{\mathrm{i}xt}\mathrm{d}t = \frac{\sin(bx)}{\pi x}, \quad \delta_{(2)}(x,b) := \frac{\pi}{b}\delta_{(1)}^{2}(x,b) = \frac{\sin^{2}(bx)}{\pi bx^{2}}. \tag{4.3}$$

The modulation factor of the grating can thus be written as

$$M = 4\pi a\frac{\sin(\eta(2N+1))}{\sin\eta}\frac{\sin(2a\eta/d)}{2a\eta/d}\delta_{(1)}(kq_{2},b), \tag{4.4}$$

where $\eta := kq_{1}d/2$. In the squared modulation factor, we substitute $\delta_{(1)}^{2} = (b/\pi)\delta_{(2)}(kq_{2},b)$. The area of the aperture is $4(2N+1)ab$. In the intensity ratios (3.25) and (3.37), the b factors in area(A) and

$\delta_{(1)}^{2}$ cancel, so that the height of the slits only enters in $\delta_{(2)}(kq_{2},b)$. Thus the $b\to\infty$ limit is well defined and gives $\delta(kq_{2})$. The principal maxima of M^{2} are determined by the interference factor, the square of the first ratio in (4.4). They are located at $\eta=n\pi$ for integer n. In between the principal intensity maxima, there are secondary ones, separated by zeros located at $\eta=n\pi/(2N+1)$, where n is integer but not a multiple of $2N+1$. The square of the second ratio in (4.4) attenuates the maxima at large η. However, since $2a/d<1$, it does not significantly affect the location of the maxima. The principal maxima occur at $\eta=n\pi$, which we may write, with $k=2\pi/\lambda$, as a Bragg condition $\mathbf{k}_{0}\mathbf{e}_{1}-\mathbf{n}\mathbf{e}_{1}=n\lambda/d$. We consider normal incidence $\mathbf{k}_{0}=\mathbf{e}_{3}$, and choose the transversal polarization vectors along the coordinate axes, $\varepsilon_{0,i}=\mathbf{e}_{i}$. In the $(\mathbf{e}_{1},\mathbf{k}_{0})$ plane orthogonal to the slits, we then have $\varphi=0$ and $\mathbf{n}\mathbf{e}_{1}=\sin\theta$, so that the principal maxima are recovered at scattering angles defined by $\sqrt{\omega^{2}+m_{\mathrm{t}}^{2}}\sin\theta=2\pi n/d$, with integer n.

4.2. Tachyon diffraction in crystal lattices: transversal and longitudinal scattering cross sections

We consider a monochromatic superluminal radiation mode, $\mathbf{E}(\mathbf{x},t)=\hat{\mathbf{E}}(\mathbf{x},\omega)\mathrm{e}^{-\mathrm{i}\omega t}+\mathrm{c.c.}$, hitting a crystal lattice, and apply this field to the electron density of the crystal. This generates a tachyonic current $\mathbf{j}(\mathbf{x},t)=qn_{\mathrm{e}}(\mathbf{x})\mathbf{v}(t)$, where $n_{\mathrm{e}}(\mathbf{x})$ is the periodic electron density in the crystal lattice. The velocity of the electrons carrying tachyonic charge q is determined by $m\dot{\mathbf{v}}=q\mathbf{E}$. (In the Heaviside–Lorentz system, $q^{2}/(4\pi\hbar c)\approx1.0\times10^{-13}$, estimated from Lamb shifts in hydrogenic ions [17].) In dipole approximation, we may neglect the spatial dependence of the amplitude $\hat{\mathbf{E}}$, so that $\mathbf{v}(t)=\hat{\mathbf{v}}(\omega)\mathrm{e}^{-\mathrm{i}\omega t}+\mathrm{c.c.}$ with $\hat{\mathbf{v}}(\omega)=\mathrm{i}q\hat{\mathbf{E}}/(\omega m)$. We thus find the Fourier amplitude of the current $\mathbf{j}(\mathbf{x},t)=\hat{\mathbf{j}}\mathrm{e}^{-\mathrm{i}\omega t}+\mathrm{c.c.}$ as [19]

$$\hat{\mathbf{j}}(\mathbf{x},\omega) = \frac{\mathrm{i}q^{2}}{m\omega}n_{\mathrm{e}}(\mathbf{x})\hat{\mathbf{E}}(\mathbf{x},\omega). \tag{4.5}$$

The inhomogeneous field equations in (2.2) read

$$\mathrm{rot}\,\hat{\mathbf{B}}+\mathrm{i}\omega\hat{\mathbf{E}} = \hat{\mathbf{j}}+m_{\mathrm{t}}^{2}\hat{\mathbf{A}}, \quad \mathrm{div}\,\hat{\mathbf{E}} = \hat{\rho}-m_{\mathrm{t}}^{2}\hat{A}_{0}, \tag{4.6}$$

where we have put $\varepsilon_{0}=\varepsilon=1$ and $\mu_{0}=\mu=1$ (vacuum permeabilities in the Heaviside–Lorentz system). The charge density follows from current conservation, $\hat{\rho}=-(\mathrm{i}/\omega)\mathrm{div}\,\hat{\mathbf{j}}$. The tachyonic radiation fields generated by current (4.5) in the crystal lattice can be split into transversally and longitudinally polarized components $\hat{\mathbf{A}}^{\mathrm{T,L}}$, like the diffracted waves (3.19). We are interested in the asymptotic radiation fields outside the crystal, determined by the current transform [28]

$$\hat{\mathbf{J}}(\mathbf{x},\omega) := \int\mathrm{d}\mathbf{x}'\hat{\mathbf{j}}(\mathbf{x}',\omega)\exp(-\mathrm{i}k(\omega)\mathbf{n}\mathbf{x}'), \tag{4.7}$$

where $k(\omega)=\sqrt{\omega^{2}+m_{\mathrm{t}}^{2}}$ is the tachyonic wave number (2.5). The projections of $\hat{\mathbf{J}}(\mathbf{x},\omega)$ onto a right-handed triad of polarization vectors $\varepsilon_{1,2}$ and $\mathbf{n}$ of the radiation field are

$$\hat{\mathbf{J}}^{\mathrm{T}(i)}(\mathbf{x},\omega) := \varepsilon_{i}(\varepsilon_{i}\hat{\mathbf{J}}(\mathbf{x},\omega)), \quad \hat{\mathbf{J}}^{\mathrm{T}}(\mathbf{x},\omega) := \hat{\mathbf{J}}^{\mathrm{T}(1)}+\hat{\mathbf{J}}^{\mathrm{T}(2)},$$
$$\hat{\mathbf{J}}^{\mathrm{L}}(\mathbf{x},\omega) := \mathbf{n}(\mathbf{n}\hat{\mathbf{J}}(\mathbf{x},\omega)), \quad \hat{\mathbf{J}} = \hat{\mathbf{J}}^{\mathrm{T}}+\hat{\mathbf{J}}^{\mathrm{L}}. \tag{4.8}$$

Here, $\mathbf{n}=\mathbf{x}/r$ is the coordinate unit vector used as longitudinal polarization vector, and $\varepsilon_{i=1,2}(\mathbf{x})$ are real transversal polarization vectors defining two degrees of linear polarization, so that ε_{i} and $\mathbf{n}$ constitute an orthonormal triad, which we choose as in (3.10). The outgoing transversal and longitudinal field components are stated in (3.19) and (3.20), where we put $\varepsilon=\mu=1$, replace the superscript T by T(i), and substitute $\hat{\mathbf{J}}^{\mathrm{T}(i),\mathrm{L}}$ as defined in (4.7) and (4.8).

We further specify the wave field incident upon the crystal as a plane wave $\hat{\mathbf{E}}(\mathbf{x},\omega)=\mathbf{E}_{\mathrm{in}}(\mathbf{k})\mathrm{e}^{\mathrm{i}\mathbf{k}\mathbf{x}}$, cf. before (3.2), generating the current $\hat{\mathbf{j}}(\mathbf{x},\omega)$ in (4.5). The polarized components $\hat{\mathbf{J}}^{\mathrm{T}(i),\mathrm{L}}(\mathbf{x},\omega)$ of the current transform (4.7) are thus found as

$$\hat{\mathbf{J}}^{T(i)} = \frac{iq^2}{m\omega} F(\mathbf{k}, \mathbf{n})(\mathbf{E}_{in}\boldsymbol{\varepsilon}_i)\boldsymbol{\varepsilon}_i, \quad \hat{\mathbf{J}}^{L} = \frac{iq^2}{m\omega} F(\mathbf{k}, \mathbf{n})(\mathbf{E}_{in}\mathbf{n})\mathbf{n},$$

$$\hat{\mathbf{J}}^{T} = \frac{iq^2}{m\omega} F(\mathbf{k}, \mathbf{n})(\mathbf{E}_{in} - (\mathbf{E}_{in}\mathbf{n})\mathbf{n}), \tag{4.9}$$

where $F(\mathbf{k}, \mathbf{n})$ denotes the scattering amplitude

$$F(\mathbf{k}, \mathbf{n}) := \int d\mathbf{x}' n_e(\mathbf{x}') \exp(i(\mathbf{k} - k(\omega)\mathbf{n})\mathbf{x}'). \tag{4.10}$$

By making use of (3.19) and (3.20), we obtain the asymptotic outgoing field strengths,

$$\hat{\mathbf{E}}_{out}^{T(i)}(\mathbf{x}, \omega) \sim -\frac{q^2}{m} \frac{e^{ik(\omega)r}}{4\pi r} F(\mathbf{k}, \mathbf{n})(\mathbf{E}_{in}\boldsymbol{\varepsilon}_i)\boldsymbol{\varepsilon}_i,$$

$$\hat{\mathbf{E}}_{out}^{L}(\mathbf{x}, \omega) \sim \frac{q^2}{m} \frac{m_t^2}{\omega^2} \frac{e^{ik(\omega)r}}{4\pi r} F(\mathbf{k}, \mathbf{n})(\mathbf{E}_{in}\mathbf{n})\mathbf{n}. \tag{4.11}$$

As for the cross sections, we start with the transversal and longitudinal flux vectors $\langle \mathbf{S}^{T(i),L} \rangle$ in (3.22), and substitute the scattered fields (3.19) and (3.20),

$$\langle \mathbf{S}_{out}^{T(i)} \rangle \sim \frac{2\omega k(\omega)}{(4\pi r)^2} |\hat{\mathbf{J}}^{T(i)}|^2 \mathbf{n}, \quad \langle \mathbf{S}_{out}^{L} \rangle \sim \frac{2m_t^2}{(4\pi r)^2} \frac{k(\omega)}{\omega} |\hat{\mathbf{J}}^{L}|^2 \mathbf{n}. \tag{4.12}$$

The squared current amplitudes (4.9) read

$$\left|\hat{\mathbf{J}}^{T(i)}\right|^2 \sim \frac{q^4}{m^2\omega^2} |F|^2 |\mathbf{E}_{in}\boldsymbol{\varepsilon}_i|^2, \quad \left|\hat{\mathbf{J}}^{L}\right|^2 \sim \frac{q^4}{m^2\omega^2} |F|^2 |\mathbf{E}_{in}\mathbf{n}|^2,$$

$$\left|\hat{\mathbf{J}}^{T}\right|^2 \sim \frac{q^4}{m^2\omega^2} |F|^2 (|\mathbf{E}_{in}|^2 - |\mathbf{E}_{in}\mathbf{n}|^2). \tag{4.13}$$

The total transversal flux $\langle \mathbf{S}^T \rangle$ is obtained by adding the transversal polarization components $\langle \mathbf{S}^{T(i)} \rangle$, which amounts to replacing the linearly polarized current transforms $\left|\hat{\mathbf{J}}^{T(i)}\right|^2$ in (4.12) by $\left|\hat{\mathbf{J}}^{T}\right|^2$ in (4.13), according to (4.8).

We also need the flux density of the incident plane wave, $\hat{\mathbf{A}}(\mathbf{x}, \omega) = \mathbf{A}_{in}(\mathbf{k})e^{i\mathbf{k}\mathbf{x}}, \hat{\mathbf{E}}(\mathbf{x}, \omega) = \mathbf{E}_{in}(\mathbf{k})e^{i\mathbf{k}\mathbf{x}}$, decomposed into transversal and longitudinal components, cf. (3.2) and (3.3). The flux carried by the transversal component, $\mathbf{k}_0\hat{\mathbf{A}}^T = 0, \hat{\mathbf{E}}^T = i\omega\hat{\mathbf{A}}^T$, reads, cf. (3.4),

$$\langle \mathbf{S}_{in}^{T} \rangle = 2\omega k(\omega)|\mathbf{A}_{in}^{T}|^2 \mathbf{k}_0 = 2\frac{k(\omega)}{\omega}|\mathbf{E}_{in}^{T}|^2 \mathbf{k}_0. \tag{4.14}$$

The longitudinal energy flux is determined by the amplitudes $\hat{\mathbf{A}}^{L} = (\hat{\mathbf{A}}^{L}\mathbf{k}_0)\mathbf{k}_0$ and $\hat{\mathbf{E}}^{L} = -im_t^2\hat{\mathbf{A}}^{L}/\omega$,

$$\langle \mathbf{S}_{in}^{L} \rangle = 2m_t^2\frac{k(\omega)}{\omega}|\mathbf{A}_{in}^{L}|^2 \mathbf{k}_0 = 2\frac{\omega k(\omega)}{m_t^2}|\mathbf{E}_{in}^{L}|^2 \mathbf{k}_0. \tag{4.15}$$

The transversal cross section for superluminal Bragg diffraction is thus found as

$$d\sigma^T = \frac{\left|\langle \mathbf{S}_{out}^{T} \rangle\right|}{\left|\langle \mathbf{S}_{in}^{T} \rangle\right|} r^2 d\Omega \sim \frac{q^4}{(4\pi)^2} \frac{|F|^2}{m^2} \left(1 - \frac{\left|\mathbf{E}_{in}^{T}\mathbf{n}\right|^2}{\left|\mathbf{E}_{in}^{T}\right|^2}\right) d\Omega, \tag{4.16}$$

where the solid angle element $d\Omega$ is centered at the outgoing wave vector $\mathbf{k}' = k(\omega)\mathbf{n}$. We may replace the factor $(1 - \left|\mathbf{E}_{in}^{T}\mathbf{n}\right|^2/\left|\mathbf{E}_{in}^{T}\right|^2)$ by $\sin^2\theta$, where θ is the angle between $\mathbf{E}_{in}^{T}$ and $\mathbf{k}'$. If the incident transversal radiation is unpolarized, we have to replace $\sin^2\theta$ by the average $(1 + \cos^2\vartheta)/2$, where ϑ is the scattering angle between the in- and outgoing wave vectors $\mathbf{k}$ and $\mathbf{k}'$. In the longitudinal cross section,

$$d\sigma^L = \frac{\left|\langle \mathbf{S}_{out}^{L} \rangle\right|}{\left|\langle \mathbf{S}_{in}^{L} \rangle\right|} r^2 d\Omega \sim \frac{q^4}{(4\pi)^2} \frac{m_t^4}{\omega^4} \frac{|F|^2}{m^2} \frac{\left|\mathbf{E}_{in}^{L}\mathbf{n}\right|^2}{\left|\mathbf{E}_{in}^{L}\right|^2} d\Omega, \tag{4.17}$$

we may replace the $\mathbf{E}_{in}^{L}$ ratio by $\cos^2\vartheta$.

In the scattering amplitude $F(\mathbf{k}, \mathbf{n})$, cf. (4.10), we write $\mathbf{k}'$ for $k(\omega)\mathbf{n}$, and substitute the Fourier series $n_e(\mathbf{x}) = \sum n_{\mathbf{G}}e^{i\mathbf{Gx}}$ over the reciprocal lattice $\mathbf{G}$,

$$F(\mathbf{k}, \mathbf{n}) = \sum_{\mathbf{G}} n_{\mathbf{G}} \int d\mathbf{x}' \exp(i(\mathbf{G} + \mathbf{k} - \mathbf{k}')\mathbf{x}'). \tag{4.18}$$

We may replace $\mathbf{G}$ by $-\mathbf{G}$ in the individual terms. The integrals in (4.18) are taken over the crystal volume, and give a sizeable contribution only if $\mathbf{k} - \mathbf{k}'$ very nearly coincides with a reciprocal lattice vector. We thus arrive at the Laue condition $\mathbf{k} - \mathbf{k}' = \mathbf{G}$, so that the respective integral just gives the crystal volume. We square $\mathbf{k}' = \mathbf{k} - \mathbf{G}$ to arrive at $2\mathbf{kG} = |\mathbf{G}|^2$, which is the diffraction condition for the incident wave vector. Alternatively, $|\mathbf{G}| = |\mathbf{k}' - \mathbf{k}| = 2k\sin(\vartheta/2)$, with scattering angle ϑ as above. The parallel lattice planes of the direct lattice orthogonal to a fixed $\mathbf{G}$ are equidistantly spaced, at distance $d = 2\pi/|\mathbf{G}_0|$, where $\mathbf{G}_0$ is the shortest reciprocal lattice vector parallel to $\mathbf{G}$, the latter being an integer multiple of $\mathbf{G}_0$, $|\mathbf{G}| = n|\mathbf{G}_0|$, cf., e.g., Ref. [30]. Replacing the wave number by frequency via the dispersion relation $k = \sqrt{\omega^2 + m_t^2}$, we find the Bragg condition for tachyon diffraction,

$$d\sin\frac{\vartheta}{2} = \frac{n\pi}{\sqrt{\omega^2 + m_t^2}}. \tag{4.19}$$

The angle $\vartheta/2$ is the glancing angle between lattice plane and wave vector; incidence and reflection angle coincide as in the electromagnetic case, irrespectively of the polarization. Owing to the negative mass-square, tachyonic Bragg diffraction can only occur at wavelengths $\lambda = 2\pi/k < 2d$, where d is usually a few Å. This matches well with the tachyonic Compton wavelength of $2\pi/m_t \approx 5.7$Å [17], which is the maximal wavelength attainable by tachyonic vacuum modes.

5. Tachyonic flare spectra of TeV blazars

Figs. 1–3 depict tachyonic cascade fits to the TeV spectra of the γ-ray blazars H2356 − 309, 1ES 1218 + 304, and 1ES 1101 − 232, obtained with imaging air Cherenkov telescopes [31]. The cascades are plots of the E^2-rescaled flux densities

$$E^2 \frac{dN^{T,L}}{dE} = \frac{\omega}{4\pi d^2} \langle p^{T,L}(\omega) \rangle, \tag{5.1}$$

where d is the distance to the source, and $\langle p^{T,L}(\omega = E/\hbar) \rangle$ the tachyonic spectral density of a uniformly moving charge [8],

$$p^{T,L}(\omega) = \frac{\alpha_q m_t^2 \omega}{\omega^2 + m_t^2} \left[\gamma^2 - \frac{m_t}{m}\frac{\omega}{m_t}\gamma - \frac{1}{4}\frac{m_t^2}{m^2} - \left(1 + \frac{\omega^2}{m_t^2}\right)\varDelta^{T,L} \right] \frac{1}{\gamma\sqrt{\gamma^2 - 1}}, \tag{5.2}$$

averaged over a thermal electron distribution. The superscripts T and L indicate the transversal and longitudinal polarization components defined by $\varDelta^T = 1 - m_t^2/(2m^2)$ and $\varDelta^L = 0$. γ is the electronic Lorentz factor, and α_q the tachyonic fine structure constant. We use the Heaviside–Lorentz system, so that $\alpha_q = q^2/(4\pi\hbar c) \approx 1.0 \times 10^{-13}$ and $m_t \approx 2.15$ keV/c^2, as inferred from Lamb-shift estimates [17]. The tachyon–electron mass ratio is $m_t/m \approx 1/238$, and a spectral cutoff occurs at

$$\omega_{max}(\gamma) = m_t\left(\mu_t\sqrt{\gamma^2 - 1} - \frac{1}{2}\frac{m_t}{m}\gamma\right), \quad \mu_t := \sqrt{1 + \frac{1}{4}\frac{m_t^2}{m^2}}. \tag{5.3}$$

Only frequencies in the range $0 \leqslant \omega \leqslant \omega_{max}(\gamma)$ can be radiated by a uniformly moving charge, the tachyonic spectral densities $p^{T,L}(\omega)$ being cut off at the break frequency ω_{max}. A positive $\omega_{max}(\gamma)$ requires Lorentz factors exceeding the threshold μ_t.

The average $\langle p^{T,L}(\omega) \rangle$ defining the differential flux (5.1) is taken over thermal ultra-relativistic electron distributions $d\rho \propto$
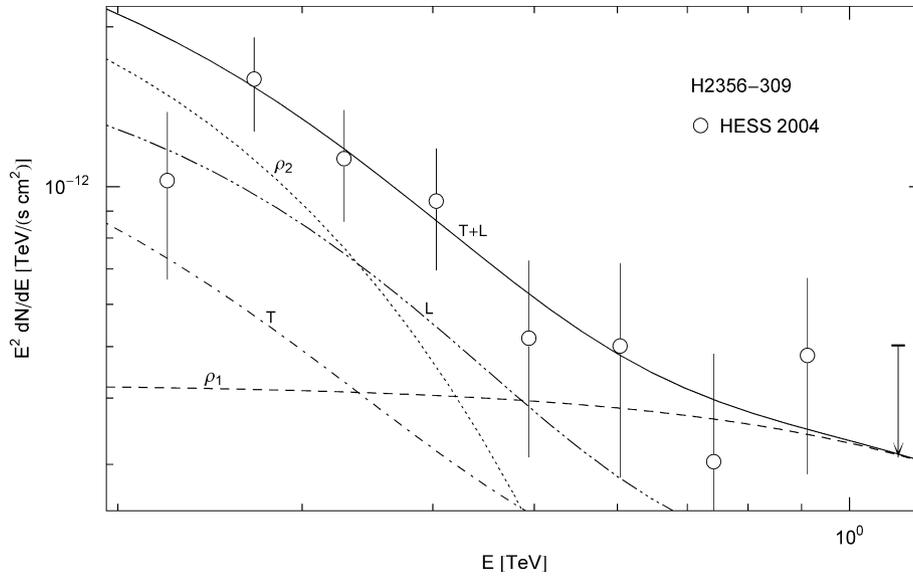
Fig. 1. Spectral map of the BL Lac object H2356 − 309. HESS data points from Ref. [31]. The solid line T + L depicts the E^2-scaled differential tachyon flux dN^{T+L}/dE, obtained by adding the flux densities $\rho_{1,2}$ of two electron populations, cf. (5.1). The transversal (T) and longitudinal (L) flux densities $dN^{T,L}/dE$ add up to the total unpolarized flux T + L. The exponential decay of the cascades $\rho_{1,2}$ sets in at about $E_{cut} \approx (m_t/m)kT$, cf. after (5.2), implying cutoffs at 0.84 TeV for the ρ_1 cascade and 92 GeV for ρ_2. The χ^2 fit is done with the unpolarized tachyon flux T + L, and subsequently split into transversal and longitudinal components. Temperature and number count of the electron populations are recorded in Table 1.
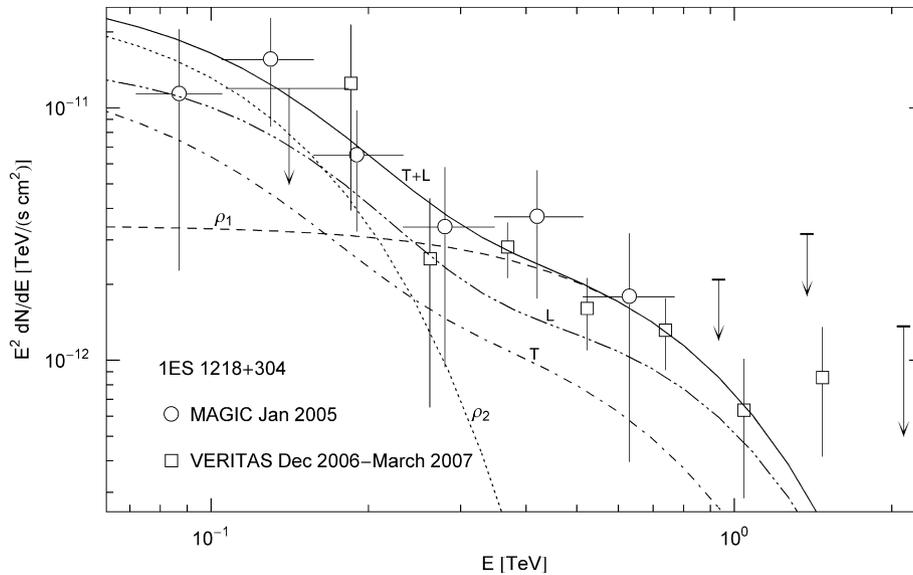
Fig. 2. Spectral map of the blazar 1ES 1218 + 304. MAGIC data points from Ref. [35], VERITAS points from Ref. [36]. The upper flux limit in the 0.1–0.2 TeV interval is based on STACEE observations in 2006 and 2007 [37]. The spectral fit T + L = ρ_1 + ρ_2 is performed with the electron distributions quoted in Table 1; the polarized flux components are labeled T and L. The ρ_1 cascade is cut at $E_{cut} \approx 0.28$ TeV, and ρ_2 at 46 GeV. Comparing to the BL Lac in Fig. 1, located at a lower redshift, there is no indication of absorption in the spectral slope. The electron densities generating the cascades $\rho_{1,2}$ are thermal in either case. The spectral curvature is intrinsic, caused by the Boltzmann factor of the electron populations in the galactic nucleus.

$e^{-\beta\gamma}\sqrt{\gamma^2 - 1}\gamma d\gamma, \beta = m/(kT)$. The least-squares fit is performed with the total unpolarized flux density $dN^{T+L} = dN^T + dN^L$. The cascades are labeled $\rho_{1,2}$ in the figures, and the parameters of the electron populations generating them are listed in Table 1. The details of the spectral fitting have been explained in Ref. [32]. The electron count is calculated as $n^e \approx 5.75 \times 10^{55}\hat{n}d^2$[Mpc], where $\hat{n}$ defines the tachyonic flux amplitude extracted from the fit. The cutoff parameter of the thermal cascades is related to the electron temperature by kT[TeV] $\approx 5.11 \times 10^{-7}/\beta$, and the internal energy estimates of the source populations in Table 1 are obtained from U[erg] $\sim 2.46 \times 10^{-6}n^e/\beta$. The distance estimates of the active

galactic nuclei are based on $d \sim cz/H_0$, with $c/H_0 \approx 4.4 \times 10^3$ Mpc. Hence, d[Mpc] $\approx 4.4 \times 10^3 z$, and $n^e \approx 1.1 \times 10^{63}\hat{n}z^2$, cf. Table 1.

Fig. 1 shows the tachyonic spectral map of the blazar H2356 − 309 at redshift $z \approx 0.165$ [31]. TeV γ-ray spectra of blazars are usually assumed to be generated by inverse Compton scattering, which results in a flux of TeV photons thought to be partially absorbed by interaction with infrared background photons, so that the intrinsic spectrum has to be reconstructed on the basis of intergalactic absorption models. By contrast, the extragalactic tachyon flux is not attenuated by interaction with the background light, there is no absorption of tachyonic γ-rays.
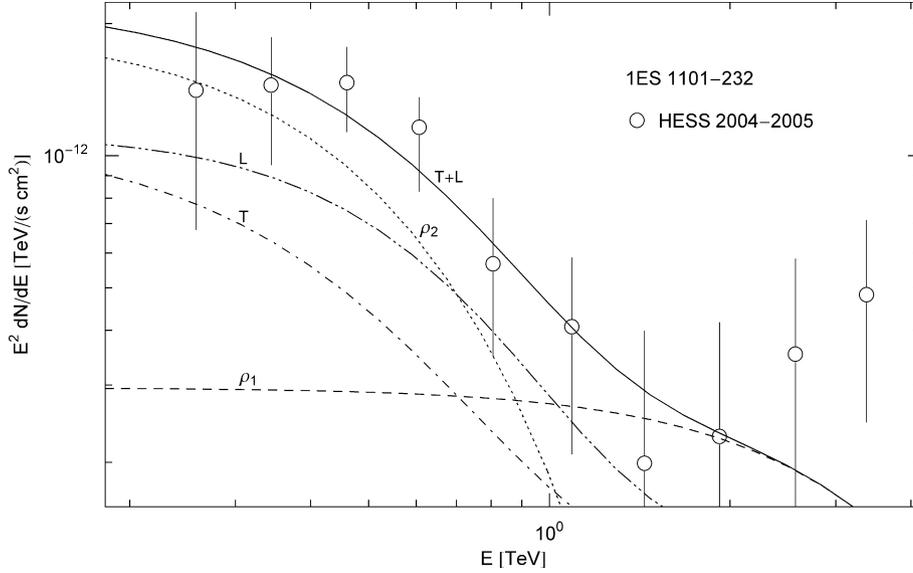
Fig. 3. Spectral map of the BL Lac object 1ES 1101 − 232. HESS flux points from Ref. [38]. The plots are labeled as in Figs. 1 and 2. The ρ_1 cascade is cut at 1.6 TeV and ρ_2 at 0.21 TeV. The parameters of the electron populations are listed in Table 1. The spectral slope is steeper than that of 1ES 1218 + 304 in Fig. 2, even though these blazars have almost identical redshifts, which suggests that the shape of the plotted density $E^2 dN^{T+L}/dE$ is intrinsic rather than affected by intergalactic absorption; tachyonic γ-rays do not interact with background photons.

Apparently, the curvature present in the TeV spectra of blazars is not correlated with distance, at least there is no evidence to that effect if we compare the spectral slopes in Figs. 1–3 to the spectral maps of other flaring active galactic nuclei such as the BL Lacertae objects (BL Lacs) H1426 + 428 ($z \approx 0.129$, 570 Mpc) and 1ES 1959 + 650 ($z \approx 0.047$, 210 Mpc) in Ref. [33], the blazars 1ES 0229 + 200 ($z \approx 0.140$, 620 Mpc) and 1ES 0347 − 121 ($z \approx 0.188$, 830 Mpc) in Ref. [32], and the quasar 3C 279 ($z \approx 0.538$, 2.4 Gpc) in Ref. [34]. Fig. 2 shows the tachyonic spectral fit of the BL Lac 1ES 1218 + 304 at $z \approx 0.182$ [35–37], and Fig. 3 the spectral map of the blazar 1ES 1101 − 232 at $z \approx 0.186$ [38]. There is no correlation between redshift and spectral curvature visible. The curvature in the spectral maps of BL Lacs is intrinsic, generated by the superluminal spectral densities of the thermal electron plasma in the active galactic nuclei [39].

6. Conclusion: tachyonic X-rays and Bragg spectrometers

We have outlined a diffraction theory of superluminal wave fields based on Kirchhoff identities, cf. Section 2, and discussed the specific case of tachyonic Bragg diffraction, first with regard to a grating aperture and then in crystal lattices, cf. Section 4. We analyzed the effect of diffraction on the polarization of tachyons, cf. Section 3, and separated the transversal and longitudinal flux components in the spectral maps of γ-ray blazars, cf. Section 5. A more detailed summary is given in the Introduction. Here, we briefly sketch how the negative mass-square shows in tachyonic X-ray spectra obtained with Bragg spectrometers.

Tachyonic spectral fits are based on the E^n-scaled flux density, cf. (5.1),

$$E^n \frac{dN}{dE} = \frac{\omega^{n-1}}{4\pi d^2} \langle p(\omega) \rangle, \tag{6.1}$$

where $\langle p(\omega) \rangle$ is the unpolarized tachyonic spectral density $p^T + p^L$ in (5.2), averaged over thermal [40,41] or nonthermal [42,43] electronic source populations. The exponent n is a conveniently chosen real power: Observational spectra are usually plotted as differential count rate dN/dE (counts per unit time, unit area, and unit energy), or differential energy flux EdN/dE (which gives the power radiated if integrated over the respective energy band), or as E^2-rescaled differential flux $E^2 dN/dE$ (energy per unit time and unit area, adopted in Section 5). If a Bragg spectrometer is used, the primary quantity measured is the flux depending on wavelength rather than energy [44]. The energy parametrization in experimental plots is done with the assumed photonic relation $\lambda = 2\pi/\omega$, which substantially differs from the tachyonic dispersion relation $\lambda = 2\pi/\sqrt{\omega^2 + m_t^2}$ in the X-ray bands, due to the tachyon mass of 2.15 keV. Therefore, we have to reparametrize the experimental spectra with the tachyonic dispersion relation before comparing to $E^n dN/dE$ in (6.1).

To this end, we start with an experimental plot of the (assumed photonic) spectral density $dP/d\lambda = \tilde{p}^{ph}(\lambda)$, parametrized by wavelength as inferred from the Bragg condition $2d\sin(\vartheta/2) = n\lambda$. The power radiated over a finite range of wavelengths is $P = \int_{\lambda_{min}}^{\lambda_{max}} \tilde{p}^{ph}(\lambda) d\lambda$. We reparametrize with energy via the photonic dispersion relation $\lambda = 2\pi/\omega_{ph}$,

$$P = \int_{\omega_{ph,min}}^{\omega_{ph,max}} p^{ph}(\omega_{ph}) d\omega_{ph}, \quad p^{ph}(\omega_{ph}) := \frac{2\pi}{\omega_{ph}^2} \tilde{p}^{ph}(2\pi/\omega_{ph}), \tag{6.2}$$

where $\omega_{ph,min} = 2\pi/\lambda_{max}$, and analogously for $\omega_{ph,max}$. (Photon frequencies are denoted by a subscript ph, to distinguish them from

Table 1
Electronic source distributions ρ_i generating the tachyonic cascade spectra of the active galactic nuclei in Figs. 1–3. Each ρ_i stands for a thermal ultra-relativistic Maxwell–Boltzmann density with cutoff parameter β in the Boltzmann factor, cf. after (5.3). $\hat{n}$ determines the amplitude of the tachyon flux generated by the electron density ρ_i, from which the electron count $n^e \propto d^2$ is inferred at the indicated distance. d is the distance to the blazar, estimated from the redshift z. kT is the temperature and U the internal energy of the electron populations ρ_i, cf. Ref. [42]. The distance estimates do not affect the spectral maps in Figs. 1–3, but the electronic source count n^e. Each cascade depends on two fitting parameters β and $\hat{n}$, extracted from the χ^2 fit T + L in the figures.

	β	$\hat{n}$	d (Mpc)	n^e	kT (TeV)	U (10^{60} erg)
H2356 − 309						
ρ_1	2.5×10^{-9}	4.6×10^{-5}	$z \approx 0.165$	1.4×10^{57}	200	1.4
ρ_2	2.3×10^{-8}	3.6×10^{-4}	730	1.1×10^{58}	22	1.2
1ES 1218 + 304						
ρ_1	7.7×10^{-9}	3.7×10^{-4}	$z \approx 0.182$	1.4×10^{58}	66	4.5
ρ_2	4.7×10^{-8}	2.9×10^{-3}	800	1.1×10^{59}	11	5.8
1ES 1101 − 232						
ρ_1	1.3×10^{-9}	3.2×10^{-5}	$z \approx 0.186$	1.2×10^{57}	390	2.3
ρ_2	1.0×10^{-8}	2.1×10^{-4}	820	8.0×10^{57}	51	2.0

their tachyonic counterpart.) By contrast, if the tachyonic dispersion relation $\lambda = 2\pi/\sqrt{\omega^2 + m_t^2}$ is used for the energy parametrization, we find $P = \int_{\omega_{\min}}^{\omega_{\max}} p(\omega) d\omega$, where

$$p(\omega) := \frac{2\pi\omega}{(\omega^2 + m_t^2)^{3/2}} \tilde{p}^{ph}\left(\frac{2\pi}{\sqrt{\omega^2 + m_t^2}}\right)$$

$$= \frac{\omega}{\sqrt{\omega^2 + m_t^2}} p^{ph}(\sqrt{\omega^2 + m_t^2}). \qquad (6.3)$$

This observationally determined tachyonic spectral density $p(\omega)$ is to be fitted with the tachyonic spectral average $\langle p(\omega) \rangle$ in (6.1). More generally, if the photonic spectral density $f_n^{ph}(\omega_{ph}) := \omega_{ph}^{n-1} p^{ph}(\omega_{ph})$ is plotted, the tachyonic density $f_n(\omega) := \omega^{n-1} p(\omega)$ is recovered as

$$f_n(\omega) = \frac{\omega^n}{(\omega^2 + m_t^2)^{n/2}} f_n^{ph}(\sqrt{\omega^2 + m_t^2}). \qquad (6.4)$$

Tachyonic and photonic frequencies are related by $\omega = \sqrt{\omega_{ph}^2 - m_t^2}$. This apparently requires $\omega_{ph} \geqslant m_t$, which is not a severe restriction, as the condition $\lambda < 2d$ for Bragg scattering in a crystal amounts to roughly the same, cf. the end of Section 4.2.

We consider a set of photonic data points $(\omega_{ph,i}, f_n^{ph}(\omega_{ph,i}))$ labeled by index i. These flux points are inferred from Bragg diffraction, that is, from the wavelength of the incident quanta, and subsequently parametrized by frequency via the photonic dispersion relation. If a tachyonic spectral fit based on density (6.1) is performed, we have to use instead the tachyonic dispersion relation for the energy parametrization. In effect, the photonic data points $(\omega_{ph,i}, f_n^{ph}(\omega_{ph,i}))$ are mapped into tachyonic points $(\omega_i, f_n(\omega_i))$ by

$$\omega_i = \omega_{ph,i}\sqrt{1 - m_t^2/\omega_{ph,i}^2},$$
$$f_n(\omega_i) = (1 - m_t^2/\omega_{ph,i}^2)^{n/2} f_n^{ph}(\omega_{ph,i}). \qquad (6.5)$$

This rescaling applies to X-ray spectra obtained from diffraction gratings. Regarding the spectral maps in Figs. 1–3, there is no need for a rescaling of the flux data, as the negative mass-square in the dispersion relation is negligible in the γ-ray bands.

Acknowledgements

References

[1] A. Sommerfeld, Proc. Konink. Akad. Wet. (Sec. Sci.) 7 (1904) 346.
[2] S. Tanaka, Prog. Theor. Phys. 24 (1960) 171.
[3] Ya.P. Terletsky, Sov. Phys. Dokl. 5 (1961) 782.
[4] R. Newton, Science 167 (1970) 1569.
[5] K. Kamoi, S. Kamefuchi, Prog. Theor. Phys. 45 (1971) 1646.
[6] R. Tomaschitz, Class. Quantum Grav. 18 (2001) 4395.
[7] R. Tomaschitz, Eur. Phys. J. D 32 (2005) 241.
[8] R. Tomaschitz, Ann. Phys. 322 (2007) 677.
[9] G. Feinberg, Phys. Rev. 159 (1967) 1089.
[10] H. Ardavan et al., J. Opt. Soc. Am. A 24 (2007) 2443.
[11] H. Ardavan et al., J. Opt. Soc. Am. A 25 (2008) 780.
[12] H. Ardavan et al., Mon. Not. R. Astron. Soc. 388 (2008) 873.
[13] A.V. Bessarab et al., Radiat. Phys. Chem. 75 (2006) 825.
[14] B.M. Bolotovskiĭ, V.L. Ginzburg, Sov. Phys. Usp. 15 (1972) 184.
[15] B.M. Bolotovskiĭ, V.P. Bykov, Sov. Phys. Usp. 33 (1990) 477.
[16] B.M. Bolotovskii, A.V. Serov, Radiat. Phys. Chem. 75 (2006) 813.
[17] R. Tomaschitz, Eur. Phys. J. B 17 (2000) 523.
[18] R. Tomaschitz, Physica A 320 (2003) 329.
[19] L.D. Landau, E.M. Lifshitz, Electrodynamics of Continuous Media, Pergamon, Oxford, 1984.
[20] M. Born, E. Wolf, Principles of Optics, Cambridge University Press, Cambridge, 2003.
[21] R. Tomaschitz, Physica B (2009), doi:10.1016/j.physb.2008.12.026.
[22] R. Tomaschitz, Physica A 307 (2002) 375.
[23] V.G. Veselago, Sov. Phys. Usp. 10 (1968) 509.
[24] A. Sommerfeld, Optics, Academic Press, New York, 1954.
[25] V.I. Tsoy, L.A. Melnikov, Opt. Commun. 256 (2005) 1.
[26] J.A. Stratton, Electromagnetic Theory, Wiley-IEEE Press, New York, 2007.
[27] J.A. Adam, Phys. Rep. 356 (2002) 229.
[28] R. Tomaschitz, Physica A 335 (2004) 577.
[29] C.J. Bouwkamp, Rep. Prog. Phys. 17 (1954) 35.
[30] R.E. Peierls, Quantum Theory of Solids, Oxford University Press, Oxford, 2001.
[31] F. Aharonian et al., Astron. Astrophys. 455 (2006) 461.
[32] R. Tomaschitz, Phys. Lett. A 372 (2008) 4344.
[33] R. Tomaschitz, Eur. Phys. J. C 49 (2007) 815.
[34] R. Tomaschitz, EPL 84 (2008) 19001.
[35] J. Albert et al., Astrophys. J. 642 (2006) L119.
[36] P. Fortin, AIP Conf. Proc. 1085 (2008) 565.
[37] R. Mukherjee et al., in: R. Caballero et al. (Eds.), Proceedings of the 30th International Cosmic Ray Conference, Meridia, Mexico, vol. 3, 2007, p. 925.
[38] F. Aharonian et al., Astron. Astrophys. 470 (2007) 475.
[39] R. Tomaschitz, EPL 85 (2009) 29001.
[40] R. Tomaschitz, Phys. Lett. A 366 (2007) 289.
[41] R. Tomaschitz, Physica A 387 (2008) 3480.
[42] R. Tomaschitz, Physica A 385 (2007) 558.
[43] R. Tomaschitz, Astropart. Phys. 27 (2007) 92.
[44] C.R. Canizares et al., Publ. Astron. Soc. Pac. 117 (2005) 1144.